Highly porous Fe_3O_4–Fe nanowires grown on C/TiC nanofiber arrays as the high performance anode of lithium-ion batteries

Kui Cheng, Fan Yang, Ke Ye, Ying Zhang, Xue Jiang, Jinling Yin, Guiling Wang, Dianxue Cao*

Key Laboratory of Superlight Material and Surface Technology of Ministry of Education, College of Material Science and Chemical Engineering, Harbin Engineering University, Harbin 150001, China

HIGHLIGHTS

- Fe_3O_4–Fe nanowires with a large amount of nanoholes directly grown on highly conductive nanofiber arrays are prepared.
- The electrode displayed remarkably high capacity, excellent high rate performance and cycling stability.
- The electrode has a satisfactory cycling performance with capacity retention of 93.9% after 100 cycles at 1C.

GRAPHICAL ABSTRACT
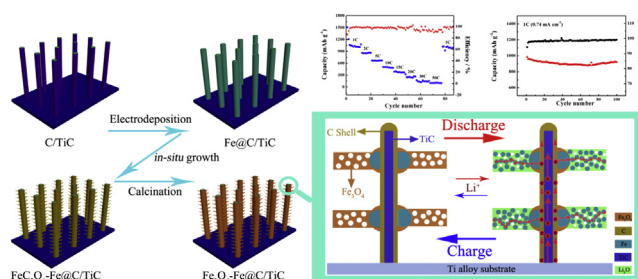
ABSTRACT

A facile and green method is developed to fabricate Fe_3O_4–Fe nanowires with a large amount of nanoholes directly grown on highly conductive nanofiber arrays. By electrodeposition of Fe clusters on C/TiC nanofiber array, followed by *in-situ* chemical conversion of Fe to FeC_2O_4–Fe nanowires and the thermal decomposition of FeC_2O_4–Fe to Fe_3O_4–Fe, a Fe_3O_4–Fe nanocomposite electrode with unique architecture is successfully prepared. The electrode is characterized by means of X-ray diffractometer, scanning electron microscope and transmission electron microscope. Electrochemical properties of the nanowire arrays electrode as the anode of lithium-ion batteries are examined by cyclic voltammetry and galvanostatic charge/discharge test. The electrode displayed remarkably high capacity, excellent high rate performance and superior cycling stability. The reversible capacity of the electrode reached 1012 mAh g^{-1} at 1C and retained to be 500 and 255 mAh g^{-1} at 10 and 20C, respectively. It can still deliver a specific capacity of 100 mAh g^{-1} even at 50C (72 s charge–discharge). The electrode also has a satisfactory cycling performance with capacity retention of 93.9% after 100 cycles at 1C. The magnificent performance can be attributed to the distinct configuration resulting from the novel fabrication process.

© 2014 Elsevier B.V. All rights reserved.

1. Introduction

To overcome the ever worsening energy and global warming issues, chemical power sources with high-specific energy and high-power density are urgently needed for electric vehicles and wind and solar energy storages. Lithium-ion batteries (LIBs) have demonstrated wide applications as electrical car power sources and large-scale green energy storage devices [1–5]. Current LIBs use graphite carbons as the anode materials, which suffer the drawbacks of limited specific capacity ($\sim$372 mAh g^{-1}) and cycling life. Therefore, new anode materials for LIBs with high capacity, long cycling lifetime and high safety are urgently demanded. Significant achievements have been gained in the research of alternative anode materials with high capacity, such as Si, intermetallic alloys

* Corresponding author. Tel./fax: +86 451 82589036.
E-mail address: caodianxue@hrbeu.edu.cn (D. Cao).

and transition metal oxides [6–14]. Recent studies show that naturally abundant, low cost, nontoxic magnetite (Fe_3O_4) displays significant promise as the anode of LIBs owing to its high capacity (924 mAh g^{-1}), nontoxicity, high corrosion resistance, high electronic conductivity (2 × 10^4 S m^{-1}) and high tap density (5.17 g cm^{-3}) [14–17]. However, the charge–discharge reaction of Fe_3O_4 (Eq. (1)) is usually accompanied by a large volume change leading to particle pulverization. As a result, the electrical connection of anode materials with current collectors can be damaged and the electrode integrity cannot be well maintained during cycling, thereby resulting in poor cycling stability [14,18–20]. Two approaches have been developed to solve this problem: synthesis of nanostructured Fe_3O_4 [21,22] and the preparation of Fe_3O_4/C composites [11,14,20,23,24].

$$Fe_3O_4 + 8Li^+ + 8e^- \leftrightarrow 3Fe + 4Li_2O \qquad (1)$$

The convectional LIBs electrode is fabricated by mixing active materials with conducting carbons and polymer binders to form a paste, which was smeared onto metal foil current collectors and pressed to thin film after evaporating solvents. This type of electrodes has a denser structure which is problematic for metal oxides anode materials having severe volume changes during lithium ion insertion/extraction because it possesses no sufficient buffering space to accommodate the electrode material expansion. The electrolyte diffusion within the electrode is also hindered. Recently, self-supported nanowire arrays directly grown on a current-collecting substrate represent an attractive architecture for Li ion battery electrode. The open space between neighboring nanowires can release strains caused by volume change and allow for easy diffusion of electrolyte into the inner region of the electrode, leading to improved cycling stability and high-power performance. Each nanowire has its own contact with the substrate at the bottom. This can ensure every nanowire to participate in the electrochemical reaction.

Herein, we reported an approach to prepare high performance Fe_3O_4 anode. Our strategy is to combine the benefits of the current collector supported array architecture, the nanostructure and the porous structure together. By a facile template-free method, porous Fe_3O_4–Fe nanowires were grown onto the core–shell C/TiC nanofibers, which form an array on Ti alloy foil current collector (Fe_3O_4–Fe@C/TiC). To the best of our knowledge, this unique structured Fe_3O_4 anode for LIBs has not been reported. Electrochemical measurements revealed that the Fe_3O_4–Fe@C/TiC nanowire array electrode exhibited a remarkably high-specific capacity and excellent cycle performance.

2. Experimental

2.1. Preparation of the shell/core C/TiC nanofiber arrays

The array of core–shell C/TiC nanofiber was synthesized according to the literature [6]. In brief, Ti6Al4V foil (10 × 10 × 1 mm^3, Advent, 99.5%) was degreased ultrasonically in acetone, ethanol and double-distilled water sequentially. The cleaned Ti6Al4V foil was loaded onto a ceramic boat and it was placed in the center of a quartz tube in a horizontal tube furnace. The tube was purged with ultrahigh purity Ar several times to remove oxygen and moisture before heating to 850 °C under Ar. Acetone was then introduced into the tube by bubbling with Ar at a flow rate of 150 sccm. After 1.5 h reaction, the array of core–shell C/TiC nanofibers was formed on the Ti alloy surface.

2.2. Preparation of the Fe_3O_4–Fe@C/TiC electrode

Fe_3O_4–Fe nanowires were directly formed on the core–shell C/TiC nanofibers via a facile deposition–immersion–calcination process. Fe particles were first electrodeposited onto the surface of C/TiC nanofibers. The deposition was performed using Autolab PGSTAT302 potentiostat (Eco Chemie) in a standard three-electrode electrochemical cell equipped with a C/TiC nanofiber array working electrode, a platinum foil counter electrode and a saturated calomel reference electrode (SCE). The deposition solution consists of 71.7 g L^{-1} FeSO$_4$·7H$_2$O and 70 mL L^{-1} triethanolamine and the deposition was carried out at a constant current of −10 mA cm^{-2} for 10 min. The obtained Fe@C/TiC was then immersed into 0.3 mol L^{-1} oxalic acid ethanol solution with 5% H$_2$O (volume ratio with H$_2$O of 5:95) for 3 h at 45 °C without stirring, and then washed with ethanol and heated at 400 °C for 120 min in a Muffle furnace to obtain the final Fe_3O_4–Fe@C/TiC electrode. The electrode morphology was characterized by a scanning electron microscope (SEM, JEOL JSM-6480) and a high-resolution transmission electron microscopy (JEOL JEM-2010F). The structure was analyzed using an X-ray diffractometer (XRD, Rigaku TTR III) with Cu $K\alpha$ radiation ($\lambda = 0.1514178$ nm).

2.3. Electrochemical measurements

The electrochemical performance of the Fe_3O_4–Fe@C/TiC electrode was measured using CR2032 coin-type half-cells. The Fe_3O_4–Fe@C/TiC was directly used as the working electrode (the mass of Fe_3O_4 is 0.8 mg cm^{-2}) without addition of binders or conducting carbon black. A Li foil was used as the reference and counter electrode. The cells were assembled in a glove box using Celgard 2400 film as the separator and 1.0 mol L^{-1} LiPF$_6$ as the electrolyte, which was dissolved in a mixture of ethylene carbonate (EC), dimethyl carbonate (DMC) and ethylene methyl carbonate (EMC) with a volume ratio of EC:DMC:EMC to be 1:1:1. Galvanostatic charge/discharge tests were performed on a Land Battery Test System (model CT2001A, China) in the potential range of 0.05–3.0 V. The cyclic voltammetry (CV) was performed on an electrochemical work-station (VMP3/Z, Bio-Logic).

3. Results and discussion

Fig. 1 shows the fabrication process of Fe_3O_4–Fe@C/TiC electrode and the corresponding XRD patterns of the sample at different preparation stages. First, arrays of C/TiC nanowires were formed on Ti alloy surface, which was used as the substrate of Fe_3O_4 active material and the current collector of the electrode due to the high electronic conductivity and excellent stability of C, TiC and Ti alloy. This substrate makes the electrode have a 3D nanowire array architecture. In the second step, Fe precursor was electrodeposited on the surface of each nanowire. Fe attached on the C/TiC nanowires was then converted to FeC$_2$O$_4$ with some Fe remaining in the junction of FeC$_2$O$_4$ and C/TiC nanowires. Finally, FeC$_2$O$_4$ was transformed to Fe_3O_4 nanowire arrays via a calcination process in the air. The XRD pattern of C/TiC nanofiber arrays is consistent with that reported in the literature [6] and the diffraction peaks can be indexed to the cubic TiC and the alloy substrate. After Fe electrodeposition, the XRD pattern shows three peaks at 44.6°, 65° and 82.3°, which can be attributed to Fe according to the JCPDS card No. 65-4899. After immersion in the oxalic acid solution, several new peaks at 18°,22°,24°,43°,50°,54° were observed, which can be ascribed to FeC$_2$O$_4$ (JCPDS card No. 14-0807). Notably, the Fe peaks still exist but their strength decreased, indicating that Fe was not completely transformed to FeC$_2$O$_4$. The remaining Fe likely exists between FeC$_2$O$_4$ and C/TiC nanowires because the formation of FeC$_2$O$_4$ starts from the outer surface and expands to the bottom of Fe particles. However, the presence of some Fe particle within the FeC$_2$O$_4$ nanowires cannot be excluded. After calcination, the peak corresponding to FeC$_2$O$_4$ disappeared and six new diffraction peaks
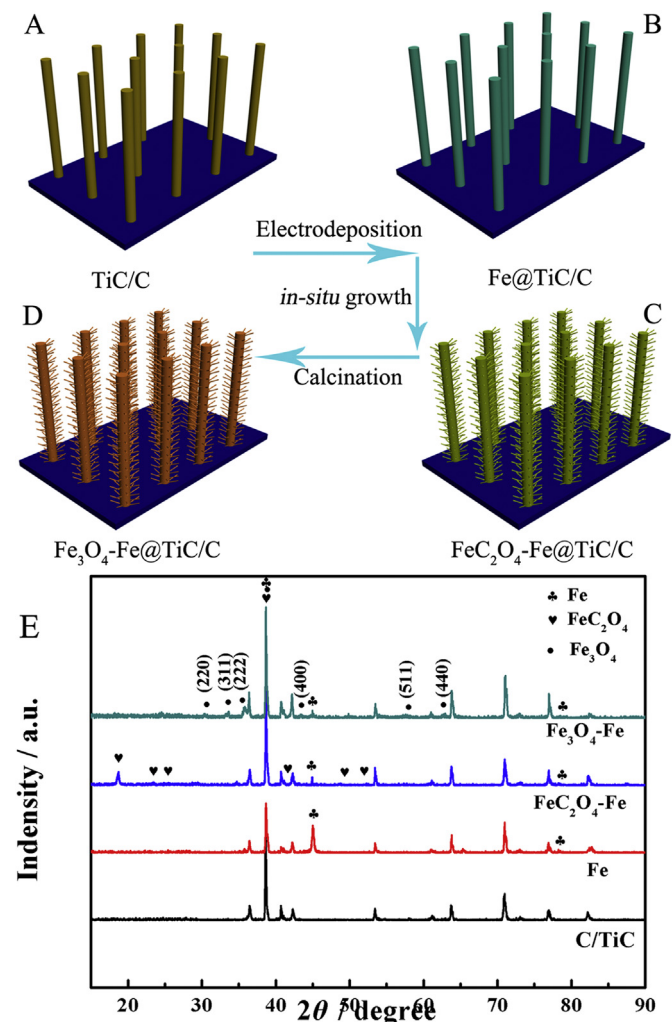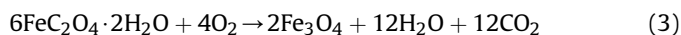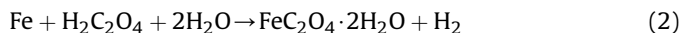
Fig. 1. Schematic illustration of the fabrication process of the Fe_3O_4–Fe@C/TiC nanowire arrays electrode (A–D) and the XRD pattern of core–shell C/TiC nanofiber arrays grown on Ti6Al4V alloy surface, Fe@C/TiC, FeC_2O_4–Fe@C/TiC, and Fe_3O_4–Fe@C/TiC (E).

at 2θ values of 30.1°, 35.4°, 37.1°, 43.1°, 57.0°, and 62.6° were observed, which matched well with the (220), (311), (222), (400), (511) and (440) planes of the spinel Fe_3O_4 (JCPDS files 65-3107; space group: F^*3 (227)) having a cubic symmetry unit cell with lattice parameters $a = b = c = 8.391$, $\alpha = \beta = \gamma = 90°$. The peaks corresponding to Fe still exist. So, it can be concluded that FeC_2O_4 was converted to Fe_3O_4 by thermal treatment while Fe remains. Possible reactions associated with the transformation of Fe to Fe_3O_4 are given below (Eqs. (2) and (3)) [25,26]:

$$Fe + H_2C_2O_4 + 2H_2O \rightarrow FeC_2O_4 \cdot 2H_2O + H_2 \quad (2)$$

$$6FeC_2O_4 \cdot 2H_2O + 4O_2 \rightarrow 2Fe_3O_4 + 12H_2O + 12CO_2 \quad (3)$$

Typical SEM and TEM images of C/TiC nanofiber, Fe@C/TiC FeC_2O_4–Fe@C/TiC, and Fe_3O_4–Fe@C/TiC are shown in Fig. 2. As seen from Fig. 2(A), C/TiC nanofibers were formed on the Ti alloy foil (Ti6Al4V) surfaces *via* a thermochemical reaction when exposed in acetone vapor at 850 °C [6]. The nanofibers pointed out of the alloy surface and covered the entire surface of Ti alloy uniformly and densely. The diameters of the nanofibers are of around 300 nm and lengths are up to several micrometers. TEM images (Fig. 2(B)) clearly show that the C/TiC nanofibers has a

core–shell structure. The diameter of TiC core is around 140 nm and the thickness of C shell is around 100 nm. Since TiC is an extremely hard material (Mohs hardness 9–9.5) with very low resistivity (6.8×10^{-5} Ω cm) [6], the core–shell C/TiC provided a stable scaffold with high surface area and high electrical conductivity. Fig. 2(C) and (D) demonstrated that the electrodeposited Fe formed clusters with diameters around 250 nm and uniformly distributed on the entire surface of each C/TiC nanofiber. Voids exist among Fe clusters, which provide rooms for the growth of FeC_2O_4 when immersed in oxalic acid solution (Fig. S1(D)). Fig. 2(E) and (G) shows the different-magnification SEM images of the Fe_3O_4–Fe@C/TiC nanowire array electrode. Clearly, all the C/TiC nanofibers were completely covered by Fe_3O_4 nanowires, which aligned vertically from the C/TiC nanofiber surface and have lengths up to around 1 μm. Fe_3O_4–Fe@C/TiC electrode has a similar morphology with that the FeC_2O_4–Fe@C/TiC electrode (Fig. S1(D)), indicating that the nanowire morphology was formed during the reaction of Fe with oxalic acid (Eq. (1)) and the structure was retained after calcinations. In order to determine the different growth stage of FeC_2O_4 nanowires from Fe nanoparticles in oxalic acid solution, the SEM images of FeC_2O_4 nanowires with the various immersing time of 1 h, 1.5 h, 2 h and 3 h were also displayed in the Fig. S1. The TEM image of Fe_3O_4–Fe@C/TiC nanowire composites (Fig. 2(F)) indicated that Fe_3O_4 nanowires wrapped on the C/TiC nanofiber and have transparent feature. Fig. 2(H) further shows that Fe_3O_4 nanowires have diameters less than around 50 nm. It is noteworthy that the Fe_3O_4 nanowires have large amount of evenly distributed nanopores with diameters ranging from 2 to 4 nm. These nanopores likely result from the release of CO_2 gas during the conversion of FeC_2O_4 into Fe_3O_4 (Eq. (3)). This special type highly porous nanowire architecture can greatly facilitate the diffusion of electrolyte within Fe_3O_4 active material, and more importantly, these numerous nanoholes provide rooms for volume expansion caused by the charge reaction of lithium ion and Fe_3O_4 (Eq. (1)), which could greatly avoid the damage of nanostructures and the occurrence of pulverization during the lithium insertion/extraction.

The excellent electrochemical performance of the Fe_3O_4–Fe@C/TiC electrode as the anode of LIB is evident from various electrochemical measurements as shown in Fig. 3. Fig. 3(A) shows the first four cyclic voltammograms (CV) of the Fe_3O_4–Fe@C/TiC electrode in the potential range of 0.05–3.0 V at a slow scan rate of 0.05 mV s^{-1}. In the initial negative-going scan (corresponding to lithiation), a weak peak at 1.0 V (*vs* Li$^+$/Li) and a strong peak at 0.55 V are observed, which are in agreement with literatures [11,20,23]. These two peaks are usually ascribed to the two lithiation reactions of Fe_3O_4 leading to the reduction of Fe^{3+} to Fe^{2+} (Eq. (4)) and Fe^{2+} to Fe^0 (Eq. (5)), as well as the side reactions occurred at the electrolyte/electrode interface resulting in the formation of SEI film [23]. The intensity of these two peaks decreased significantly in the second cycle, and the cathodic peaks finally stabilized at 0.69 V and 1.34 V after around 3 cycles, indicating the end of irreversible reactions corresponding to the formation of SEI film. The anodic peaks at 1.54 and 2.12 V can be attributed to the oxidation of Fe^0 to Fe^{2+}/Fe^{3+} accompanying lithium ion extraction (delithiation).

$$Fe_3O_4 + 2Li^+ + 2e^- \rightarrow Li_2(Fe_3O_4) \quad (4)$$

$$Li_2(Fe_3O_4) + 6Li^+ + 6e^- \rightarrow 3Fe + 4Li_2O \quad (5)$$
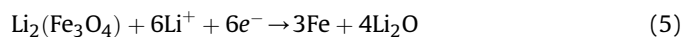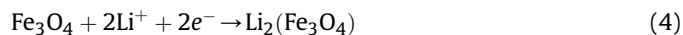
Fig. 3(B) shows the charge–discharge curves of the initial four cycles at a current rate of 1C between 0.05 and 3.0 V. The first discharge curve shows an extended potential plateau at about 0.8 V comparing to subsequent discharge curves, which is in good
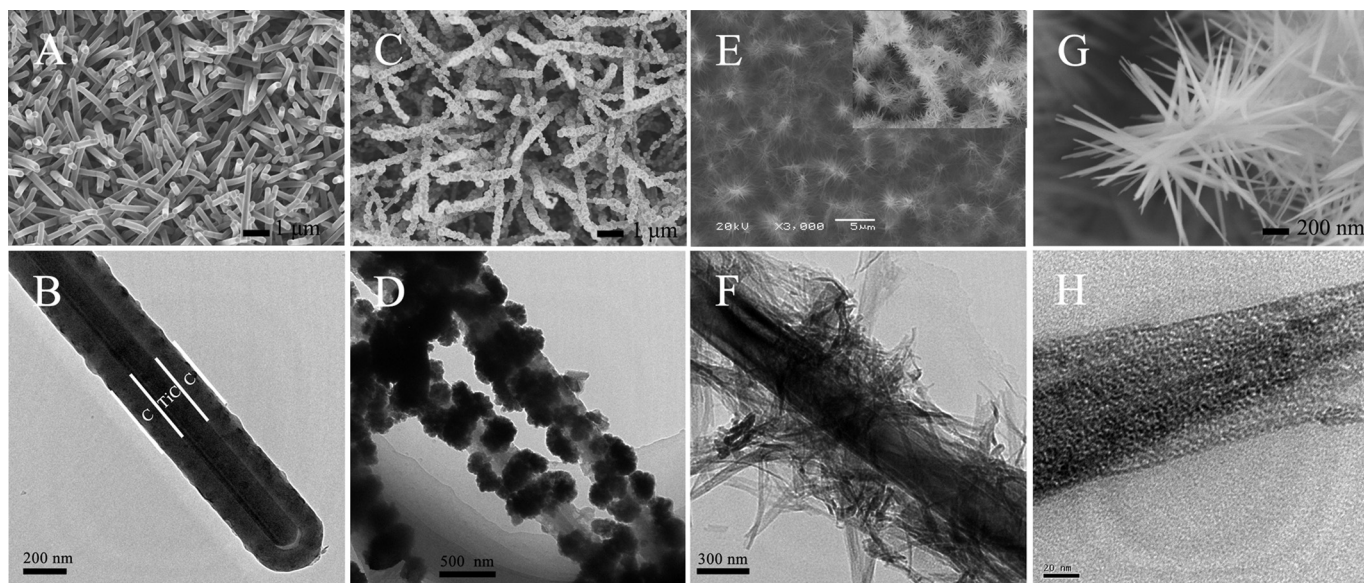
Fig. 2. SEM images of C/TiC nanofiber arrays (A), Fe@C/TiC array (C), and Fe₃O₄−Fe@C/TiC array (E, G). TEM images of C/TiC nanowire (B), Fe@C/TiC nanowire (D), Fe₃O₄−Fe@C/TiC nanowire composites (F), and Fe₃O₄ nanowire (H).

agreement with literature results for Fe_3O_4 [15,23]. The initial discharge specific capacity of the Fe_3O_4−Fe reached as high as 1511 mAh g^{-1}, but, corresponding to an initial Coulombic efficiency of around 85.8%, which is higher than that of carbon coated (or encapsulated) nanosized Fe_3O_4 [11,20,23]. The initial capacity loss is likely caused by the electrolyte decomposition and SEI formation,

which are common to most anode materials. This discharge behavior is consistent with the CV results (Fig. 2(A)), which shows a large cathodic peak in the first scan and it significantly decreased in the subsequent cycles. The discharge capacities of the electrode in second and third cycles are 1205 and 1063 mAh g^{-1}, respectively, and the fourth discharge curve overlaps with the third cycle,
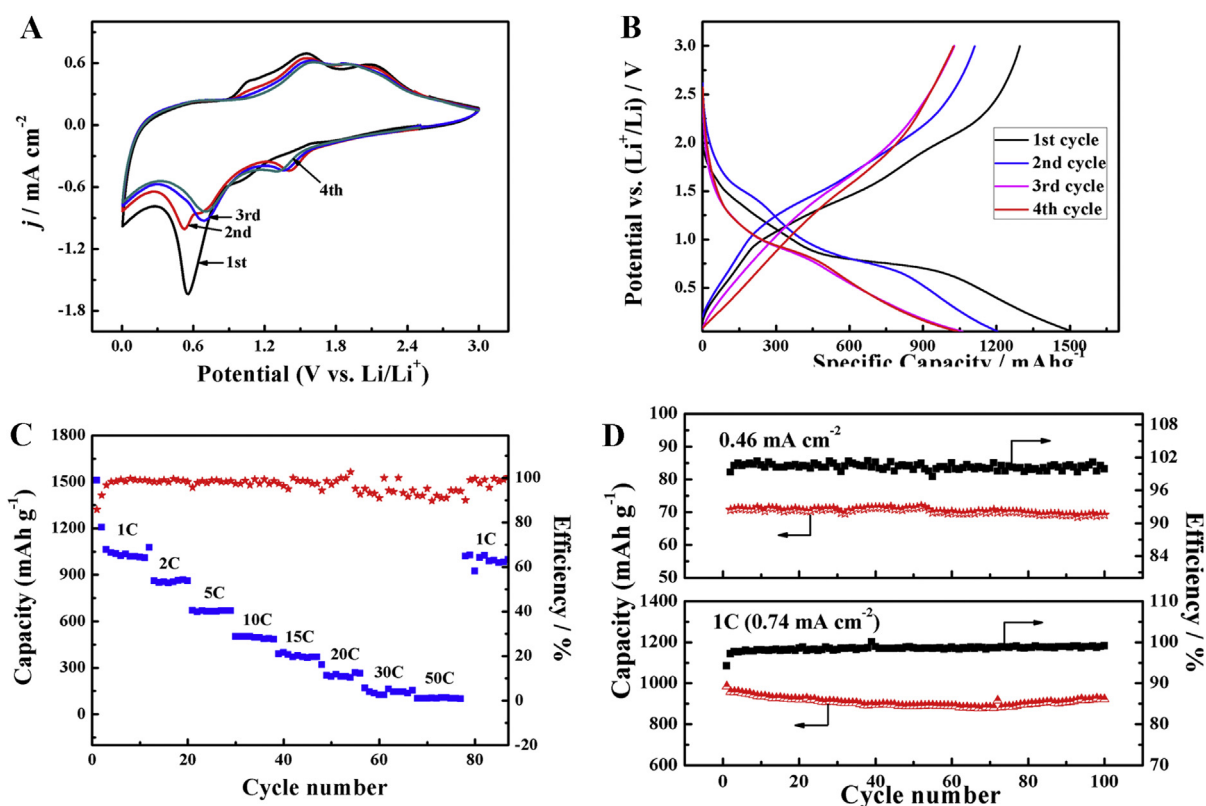

Fig. 3. Cyclic voltammograms of the Fe_3O_4−Fe@C/TiC electrode at a scan rate of 0.05 mV s^{-1} (A). Charge−discharge curves of the Fe_3O_4−Fe@C/TiC electrode at 1C (B). Rate capacity of the Fe_3O_4−Fe@C/TiC electrode in the potential range of 0.05−3.0 V (C). Cycling performance of the C/TiC nanofiber arrays substrate and the Fe_3O_4−Fe@C/TiC (D).

implying the SEI film formation and other side reactions are completed.

In addition to the high-specific capacity, the 3D Fe_3O_4–Fe@C/TiC electrode also exhibited excellent high rate performance. Fig. 3(C) shows the dependence of specific capacity and charge/discharge efficiency on the current rates. The electrode delivers a discharge capacity of 1012 mAh g^{-1} after first repetitive charge–discharge at 1C for 10 times. The specific capacity retained to be 860, 667, 500, 370, and 255 mAh g^{-1} after further charge–discharge at 2, 5, 10, 15 and 20C each for 10 times, respectively. Even at a high rate of 50C (72 s charge–discharge), the electrode can still deliver a specific capacity of 100 mAh g^{-1}. After a total of 80 cycles at various rates, the charge–discharge rate was set back to its initial value of 1C and the electrode was further cycled for 10 times, a specific capacity of 1034 mAh g^{-1} was achieved, which is around 100% of that after the first 10 cycles at 1C. This result indicated that the Fe_3O_4–Fe@C/TiC electrode has excellent high rate performance and is sustainable to high rate charge–discharge. Such properties are very important for LIBs to be charged quickly and to be able to generate high-power output also. The Coulombic efficiency in the first cycles at 1C is 85.8%, and it increased to and maintained at around 100% during the subsequent 87 cycles at different rates. The low efficiency in the initial three cycles might result from the SEI formation, as demonstrated by CV measurements (Fig. 3(A)).

To further highlight the cycling stability, the Fe_3O_4–Fe@C/TiC electrode was subjected to charge–discharge at 1C for 100 cycles (Fig. 3(D)). As seen, a high capacity of 921.3 mAh g^{-1} was retained after 100 cycles, which is about 93.9% of the initial reversible capacity (981 mAh g^{-1}) and close to the theoretical value. This capacity retention is much better than that of commercial Fe_3O_4 nanoparticles and is comparable with carbon coated or encapsulated Fe_3O_4 nanoparticle and Fe_3O_4/graphene composite [11,20,23,27]. The Coulombic efficiency maintained at nearly 100% during the entire cycling process except the first few cycles, suggesting a facile lithium insertion/extraction associated with efficient transport of ions and electrons in the electrodes. In order to determine the stability of the C/TiC nanofiber arrays and eliminate the influence of the substrate (due to the C coating), we also examined the cycle performance of C/TiC nanofiber arrays electrode at the current density of 0.46 mA cm^{-2} (Fig. 3(D)). It can be seen that C/TiC nanofiber arrays electrode exhibits excellent cycling stability and also provides a certain amount of specific capacity (70 mAh g^{-1}), which is much smaller than that provided by the active material Fe_3O_4.

The excellent high rate capability and cycling stability of the Fe_3O_4–Fe@C/TiC electrode was discussed using the illustration shown in Fig. 4. It has been reported that when Fe_3O_4 is reduced completely into Fe by lithium (Eq. (1)) during charge process, the volume increase theoretically by 80.8% [20]. Such a large volume expansion and shrinkage can lead to the pulverization of the Fe_3O_4 particles and destroy the electrode integration, which is believed to be the major factor leading to the poor cycling stability of Fe_3O_4. Our Fe_3O_4–Fe@C/TiC electrode exhibited an excellent cycling stability, which can be attributed to its novel configuration and the highly porous structure. First, Fe_3O_4 is nanowire with a diameter less than around 50 nm, which diminished the effect of volume change comparing to large particles. Secondly, every Fe_3O_4 nanowire has a porous structure with significant amount of nanoholes uniformly distributed in the entire nanowire. These pores provide enough spaces to accommodate the volume change during the lithiation/delithiation processes and maintain the nanowire integrity. Thirdly, the void among Fe_3O_4 nanowires also allows the nanowire to swell without mechanical interaction. Besides, the SEM image of Fe_3O_4–Fe@C/TiC electrode after cycling test was also exhibited in Fig. S2. It can be seen that the electrode after cycling
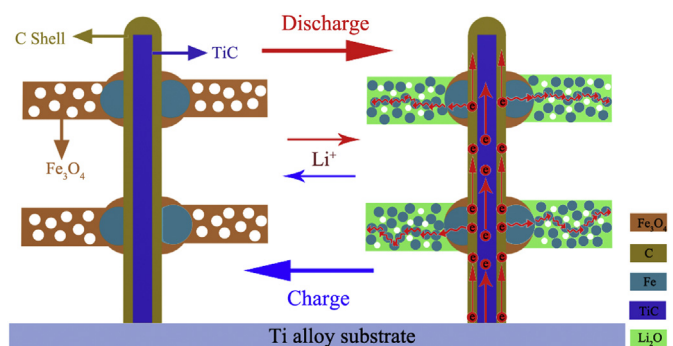

Fig. 4. Schematic illustration of the volume change buffering during charge and discharge process of the Fe_3O_4–Fe@C/TiC electrode.

test also maintained the original morphology, except for the aggregation of the Fe_3O_4 nanowires, indicating that the as-prepared electrode has superior stability during the reaction progress. The high rate performance of the Fe_3O_4–Fe@C/TiC electrode might be due to the following reasons: (1) All the Fe_3O_4 nanowires directly grown on the highly conductive C/TiC nanofibers (*via* Fe particles probably), thus the resistance of electron transportation from current collector to active material is significantly reduced because the diminished contact resistance between Fe_3O_4 and C/TiC; (2) The Fe_3O_4 nanowires have diameters less than around 50 nm, and very nanowire has a large amount of uniformly distributed nanoholes. This highly porous nanostructure remarkably increased the contact area of Fe_3O_4 with electrolyte and shortened the diffusion path of Li ions to and in Fe_3O_4. Besides, the nanowire array configuration also favors the transportation of electrolytes to the active materials.

In a very recent paper, He et al. [14] made a comprehensive comparison about the specific capacity at different rates for nano-structured Fe_3O_4 and Fe_3O_4/C composite anodes reported in the literatures. They found that, among all the Fe_3O_4 electrodes studied so far, the Fe_3O_4@C@PGC nanosheets composite displayed the best performance, followed by the Fe_3O_4/graphene composite [28,29] and the Fe_3O_4 nanoparticles confined in mesocellular carbon foam [30]. We summarized the high rate performance of these Fe_3O_4 anodes and compared with our Fe_3O_4–Fe@C/TiC nanowire arrays electrode (Table 1). As seen, the high rate performance of our Fe_3O_4–Fe@C/TiC nanowire arrays electrode is comparable with the Fe_3O_4@C@PGC nanosheets composite, and significantly higher than other Fe_3O_4 electrode previously reported. So this work demonstrated that the highly porous nanowires of Fe_3O_4–Fe are promising anode materials for LIBs with high capacity, excellent high rate capability and superior cycling stability.

4. Conclusions

High performance Fe_3O_4–Fe@C/TiC nanowire array anode for LIBs was successfully fabricated *via* a facile process by electrodeposition of Fe on conductive substrates, followed by *in-situ*

Table 1
Comparison of the specific capacity at different rates for nanostructured Fe_3O_4 anodes.

Discharge rates	1C	5C	10C	20C	50C	Ref.
Fe_3O_4@C@PGC nanosheet composite (mAh g^{-1})	963	868	570	297	–	[14]
Fe_3O_4/graphene nanocomposite (mAh g^{-1})	900	500	–	–	–	[28,29]
Fe_3O_4 nanoparticles confined in mesocellular carbon foam (mAh g^{-1})	740	475	175	–	–	[30]
Fe_3O_4–Fe@TiC/C nanowire arrays (mAh g^{-1})	1012	667	500	255	100	This work

chemical reaction with oxalic acid and final thermal conversion. The electrode has a unique hierarchical structure and the Fe_3O_4–Fe nanowires are highly porous with diameters less than around 50 nm in diameter. This special architecture endows the electrode with large contact area between Fe_3O_4 and electrolyte, short diffusion path for lithium ion transportation to and in the active material, low electron transfer resistance from current collector to active material (low contact resistance), and superior buffering ability for the volume changes during charge and discharge processes. Consequently, the electrode exhibited remarkably high capacity, excellent high rate performance and cycling stability. The discharge capacity at 10 and 50C rates reached 500 and 100 mAh g^{-1}, respectively. The capacity loss is less than 6.4% after 100 cycles at the rate of 1C.

Acknowledgments

Appendix A. Supplementary data

Supplementary data related to this article can be found at http://dx.doi.org/10.1016/j.jpowsour.2014.02.038.

References

[1] G. Ferrara, L. Damen, C. Arbizzani, R. Inguanta, S. Piazza, C. Sunseri, M. Mastragostino, J. Power Sources 196 (2011) 1469–1473.
[2] M.V. Reddy, T. Yu, C.H. Sow, Z.X. Shen, C.T. Lim, G.V. Subba Rao, B.V.R. Chowdari, Adv. Funct. Mater. 17 (2007) 2792–2799.
[3] M. Armand, J.M. Tarascon, Nature 451 (2008) 652–657.
[4] J.M. Tarascon, M. Armand, Nature 414 (2001) 359–367.
[5] Z. Zhang, H. Chen, X. She, J. Sun, J. Teo, F. Su, J. Power Sources 217 (2012) 336–344.
[6] Y. Yao, K. Huo, L. Hu, N. Liu, J.J. Cha, M.T. McDowell, P.K. Chu, Y. Cui, ACS Nano 5 (2011) 8346–8351.
[7] H. Zhou, S. Zhu, M. Hibino, I. Honma, M. Ichihara, Adv. Mater. 15 (2003) 2107–2111.
[8] J. Hassoun, S. Panero, P. Simon, P.L. Taberna, B. Scrosati, Adv. Mater. 19 (2007) 1632–1635.
[9] Y. Yu, L. Gu, X. Lang, C. Zhu, T. Fujita, M. Chen, J. Maier, Adv. Mater. 23 (2011) 2443–2447.
[10] X. Xia, J. Tu, Y. Zhang, J. Chen, X. Wang, C. Gu, C. Guan, J. Luo, H.J. Fan, Chem. Mater. 24 (2012) 3793–3799.
[11] W.-M. Zhang, X.-L. Wu, J.-S. Hu, Y.-G. Guo, L.-J. Wan, Adv. Funct. Mater. 18 (2008) 3941–3946.
[12] S. Venkatachalam, H. Zhu, C. Masarapu, K. Hung, Z. Liu, K. Suenaga, B. Wei, ACS Nano 3 (2009) 2177–2184.
[13] P.F. Teh, S.S. Pramana, Y. Sharma, Y.W. Ko, S. Madhavi, ACS Appl. Mater. Inter. 5 (2013) 5461–5467.
[14] C. He, S. Wu, N. Zhao, C. Shi, E. Liu, J. Li, ACS Nano 7 (2013) 4459–4469.
[15] D. Su, H.-J. Ahn, G. Wang. J. Power Sources.
[16] P. Wang, M. Gao, H. Pan, J. Zhang, C. Liang, J. Wang, P. Zhou, Y. Liu, J. Power Sources 239 (2013) 466–474.
[17] S. Jin, H. Deng, D. Long, X. Liu, L. Zhan, X. Liang, W. Qiao, L. Ling, J. Power Sources 196 (2011) 3887–3893.
[18] P.L. Taberna, S. Mitra, P. Poizot, P. Simon, J.M. Tarascon, Nat. Mater. 5 (2006) 567–573.
[19] P. Poizot, S. Laruelle, S. Grugeon, L. Dupont, J.M. Tarascon, Nature 407 (2000) 496–499.
[20] L. Wang, Y. Yu, P.C. Chen, D.W. Zhang, C.H. Chen, J. Power Sources 183 (2008) 717–723.
[21] N. Kang, J.H. Park, J. Choi, J. Jin, J. Chun, I.G. Jung, J. Jeong, J.-G. Park, S.M. Lee, H.J. Kim, S.U. Son, Angew. Chem. Int. Ed. 51 (2012) 6626–6630.
[22] Z.-M. Cui, L.-Y. Jiang, W.-G. Song, Y.-G. Guo, Chem. Mater. 21 (2009) 1162–1166.
[23] T. Zhu, J.S. Chen, X.W. Lou, J. Phys. Chem. C 115 (2011) 9814–9820.
[24] G. Zhou, D.-W. Wang, F. Li, L. Zhang, N. Li, Z.-S. Wu, L. Wen, G.Q. Lu, H.-M. Cheng, Chem. Mater. 22 (2010) 5306–5313.
[25] J. Xu, J. Cai, J. Wang, L. Zhang, Y. Fan, N. Zhang, H. Zhou, D. Chen, Y. Zhong, H. Fan, H. Shao, J. Zhang, C.-n. Cao, Electrochem. Commun. 25 (2012) 119–123.
[26] R. Amutha, S. Akilandeswari, M. Muruganandham, Mika Sillanp, B. Ahmmad, T. Ohkubo, J. Nanosci. Nanotechnol. 11 (2011) 3171–3179.
[27] A. Hu, X. Chen, Y. Tang, Q. Tang, L. Yang, S. Zhang, Electrochem. Commun. 28 (2013) 139–142.
[28] W. Chen, S. Li, C. Chen, L. Yan, Adv. Mater. 23 (2011) 5679–5683.
[29] Y. Su, S. Li, D. Wu, F. Zhang, H. Liang, P. Gao, C. Cheng, X. Feng, ACS Nano 6 (2012) 8349–8356.
[30] E. Kang, Y.S. Jung, A.S. Cavanagh, G.-H. Kim, S.M. George, A.C. Dillon, J.K. Kim, J. Lee, Adv. Funct. Mater. 21 (2011) 2430–2438.